Journal of Manufacturing Processes 37 (2019) 321–331

Contents lists available at ScienceDirect

Journal of Manufacturing Processes

journal homepage: www.elsevier.com/locate/manpro

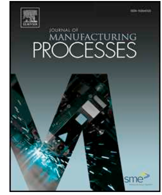

Effects of tool rake angle and tool nose radius on surface quality of ultraprecision diamond-turned porous silicon

Mehdi Heidari[a,b,*], Javad Akbari[a], Jiwang Yan[b,*]

[a] *School of Mechanical Engineering, Sharif University of Technology, Tehran, 14588-89694, Iran*

[b] *Department of Mechanical Engineering, Keio University, 3-14-1 Hiyoshi, Kohoku-ku, Yokohama, 223-8522, Japan*

A R T I C L E   I N F O

Keywords:
Porous materials
Single-crystal silicon
Tool rake angle
Tool nose radius
Ultraprecision cutting
Diamond turning
Surface quality

A B S T R A C T

This paper presents an investigation of the effects of tool rake angle and nose radius on the surface quality of ultraprecision diamond-turned porous silicon. The results showed that as rake angle decreases, the high-stress field induced by the tool edge increases, causing microcracks to propagate extensively near the pore walls. As a result, the ductile-machined areas shrank under a negative tool rake angle. On the other hand, brittle fracture occurred around pores released cutting pressure significantly. These trends of rake angle effects are distinctly different from those in the cutting of non-porous silicon. Finite element simulation of stress in the cutting area agreed with the experimental results. The results also indicated that using a tool with a bigger nose radius suppressed brittle fractures around the pore edge and improved surface quality. Raman spectroscopy of the ductile-machined surfaces revealed that the amorphization of the subsurface layer became more significant when decreasing tool rake angle or increasing tool nose radius. By choosing the optimal tool geometry, a high quality surface can be achieved on porous silicon, which demonstrates the capability of the diamond turning process to fabricate high-precision components.

1. Introduction

With the introduction of porous structures in biomedical technology over the past decades, porous materials have been the subject of an increasing amount of interest and research effort in both academia and industry. Nowadays, porous materials are the potential materials for various medical and industrial applications where, in addition to requirements for complex shapes, other characteristics such as porosity and surface topography have a profound impact on their applications. These special structures are produced in different base materials for a wide variety of applications. Single crystal silicon is a very interesting base-material for this purpose due to unique thermal and physical properties [1]. Characteristics such as controllable pore sizes, the large surface area within a small volume and its suitable dielectric property with active surface chemistry [2] make porous silicon a very promising material not only for optics but also for acoustics, medical therapy, nutrition, diagnostics, energy conversion and, cosmetics. Moreover, because of its high theoretical capacity and a high wide absorption band and transmission, recently porous silicon has attracted more attention in Li-ion batteries and solar cell applications respectively [3–8].

Regarding the uneven surface of porous silicon produced during the anodization of a single-crystal silicon wafer, it is essential to be cut precisely into various shapes for different applications. During conventional machining of porous parts, structural changes may take place typical for porous materials only, such as variations in their state of the interparticle contacts and density. As a result, choosing the best method is a great challenge. It is expected that high-precision fabrication technologies are able to meet these requirements.

There are increasing reports on precision turning of various porous materials, such as porous silicon [9], titanium [10], and tungsten [11,12]. In a previous study by the present authors, the possibility of direct fabrication of precision surfaces using a single-crystal diamond tool in turning porous silicon had been presented. The results indicated that the presence of pores significantly changes the mechanism of cutting in porous silicon compared to bulk silicon. The role of hydrostatic pressure on brittle fracture around pore was shown [9]. However, up to date, the effects of changes in tool geometry on the stress field and cutting mechanism as well as its influence on surface topography have not been investigated yet.

In this paper, the effects of tool rake angle and tool nose radius on the stress field induced by tool cutting edge and its influence on brittle fracture around pores have been investigated. Experimental results were then compared with finite element (FE) simulation and Raman spectroscopy tests. The results of this work will assist establishing

* Corresponding authors.
E-mail addresses: heidarimehdi@keio.jp, heidari@sharif.edu (M. Heidari), yan@mech.keio.ac.jp (J. Yan).

https://doi.org/10.1016/j.jmapro.2018.12.003
Received 13 September 2018; Received in revised form 30 November 2018; Accepted 1 December 2018
1526-6125/ © 2018 The Society of Manufacturing Engineers. Published by Elsevier Ltd. All rights reserved.

Downloaded from Yan Laboratory, Keio University at http://www.yan.mech.keio.ac.jp. Redistribution is subject to copyright licence from the journal publisher.

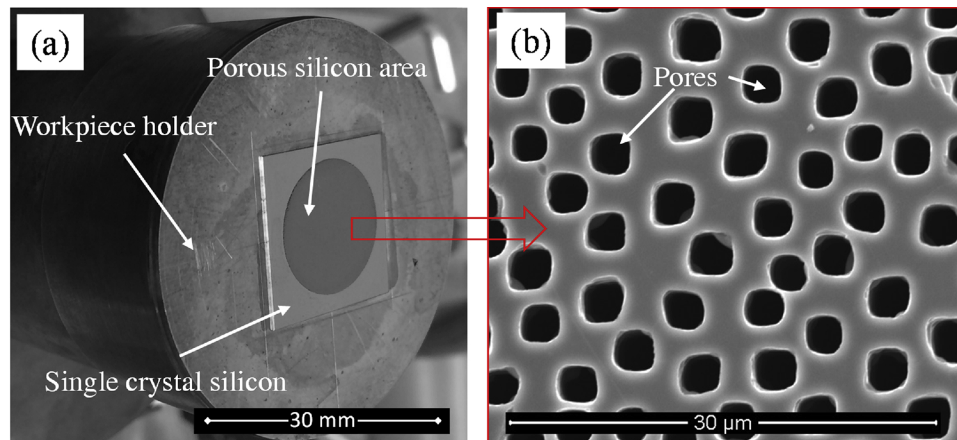

Fig. 1. Porous silicon workpiece.

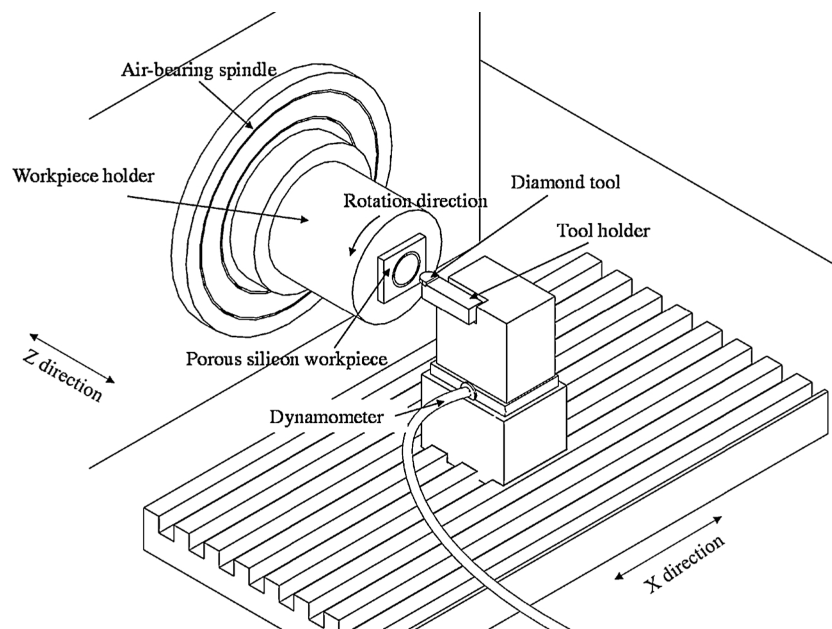

Fig. 2. Schematic diagram of the experimental setup.

process criteria in term of tool geometry for the ultraprecision cutting of porous silicon functional products for various applications.

2. Experimental and simulation procedures

2.1. Workpiece material

Several samples of porous single crystal silicon with the same size of 20.0 mm × 20.0 mm and a thickness of 330 µm were used as workpieces in this study (Fig. 1a). Porous silicon samples had 16 mm diameter of porous zone with blind pores and 2.7 µm average pore size (Fig. 1b). The workpiece was bonded onto a holder (copper blank) using a wax. The holder was then fixed onto an air-bearing spindle. The anodic oxidation process was used to fabricate porous silicon from single-crystal silicon (100) wafers.

2.2. Experimental setup

In the present work, the experiments were conducted in the face turning process using an ultraprecision lathe machine, NACHI ASP-15 (NACHI-FUJIKOSHI CORP). Fig. 2 shows a schematic diagram of the experimental setup. The machine was equipped with two perpendicular linear tables driven by servomotors and a spindle with the ultraprecision air-bearing. To prevent backlash movements, hydrostatic bearings, driven by a friction drive, support machine rotary table. In addition, to accurately position all tables, the laser hologram scales are used.

2.3. Cutting tool and cutting model

Single-crystal diamond tools (commercially available) with a nose radius of 1.0 mm, rake and clearance angles of 0° and 6°, respectively, were used in the experimental tests as the main tools. In order to

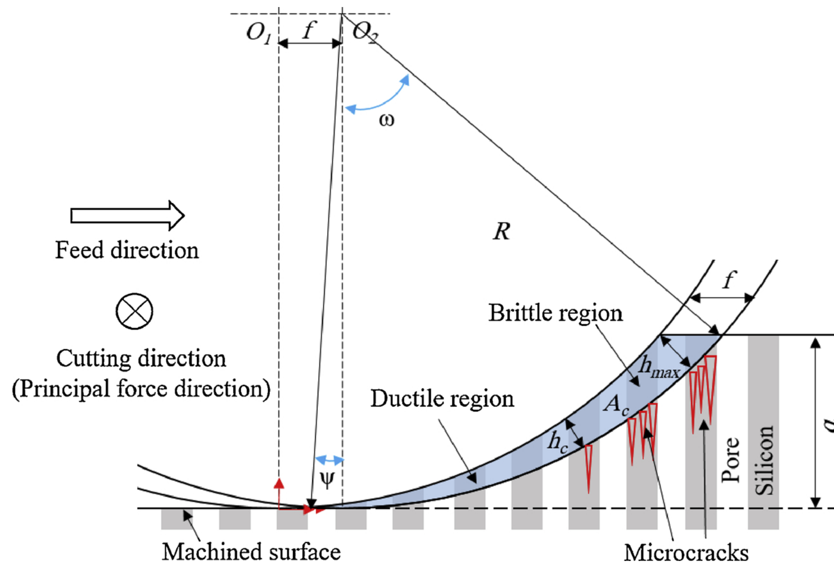

Fig. 3. Schematic model for diamond turning with a round-nosed tool.

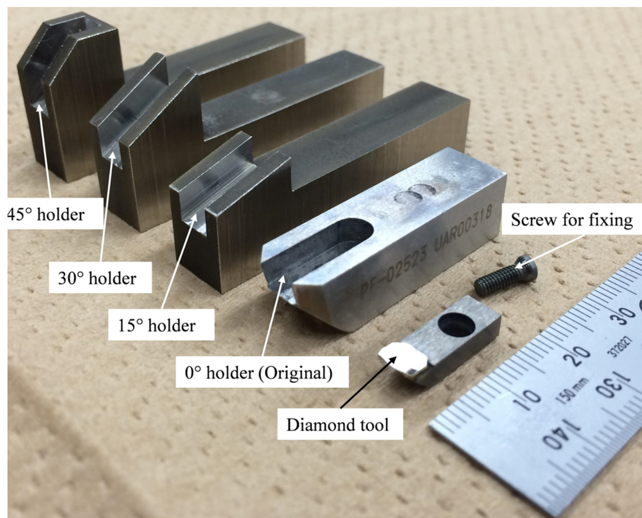

Fig. 4. Tool holders for rake angle adjustment.

consider the effects of tool nose radius on surface, two other tools with the nose radii of 0.5 mm and 10.0 were applied. Fig. 3 shows the schematic diagram of chip formation in the diamond turning process with a round-nosed tool. The figure also shows an important parameter, the maximum undeformed chip thickness $h_{\max}$, which is used to evaluate the cutting performance in ultraprecision turning. $h_{\max}$ can be calculated using the following equation when $f < \sqrt{2Ra - a^2}$ [13,14].

$$h_{max} = R - \sqrt{R^2 + f^2 - 2f\sqrt{2Ra - a^2}} \tag{1}$$

Where R is tool nose radius, a is the depth of cut and f is tool feed rate. When $f \geq \sqrt{2Ra - a^2}$, however, $h_{\max}$ is equal to the depth of cut a.

To survey the influences of tool rake angle on the mechanism of cutting, in addition to the original holder of the tool, three other tool holders having various slopes were designed to enable rake angles of −15°, −30° and −45°, as shown in Fig. 4. Thus, in all the tests, the same diamond inserts with 0° rake angle were used. It is worth noting that changing tool rake angle using angled tool holders will change the clearance angle too. Usually for the same rake angle, a tool with a bigger clearance angle results in a lower temperature rise in silicon cutting and reduces the cutting force [15]. In this study, clearance angle is increased with decreasing the rake angle. This will cause reduction of temperature and cutting force, which is opposite to the effect of tool rake angle. Moreover, in this study all experiments were conducted at a low cutting speed to eliminate the effects of heat-induced material softening.

Table 1
FEM modeling parameters of the workpiece.

Parameters	Value
Pressure-sensitivity coefficient	0.375
Hardness (GPa)	13.0
Tensile yield stress (GPa)	5.9
Fracture strain (%)	0.025
Fracture toughness (MPa $\sqrt{m}$)	1.2
Young's modulus (GPa)	165
Thermal Conductivity (W/m ^{0} C)	149
Heat Capacity, J/kg ^{0}C	712
Density, kg/m^3	233

2.4. Machining conditions

The circular concentric areas were cut on each sample at different feed rates of 0.5, 2.0 and 5.0 μm/rev with the depth of cut ranged from 1 to 4 μm. The cutting speed was fixed on the low value of 12.0 m/min to reduce its effects on material deformation in terms of heat-induced material softening [16]. Regarding the machining conditions used in this study, the maximum undeformed chip thickness h_{max} ranged approximately from 7 to 700 nm.

2.5. Measurement apparatus

In order to observe the sample surfaces a field-emission scanning electron microscope (FE-SEM, Model JSM-7600 F, JEOL) and a scanning electron microscope (SEM, Model Inspect S50) were used. To characterize the subsurface damage a Laser micro-Raman spectroscope,

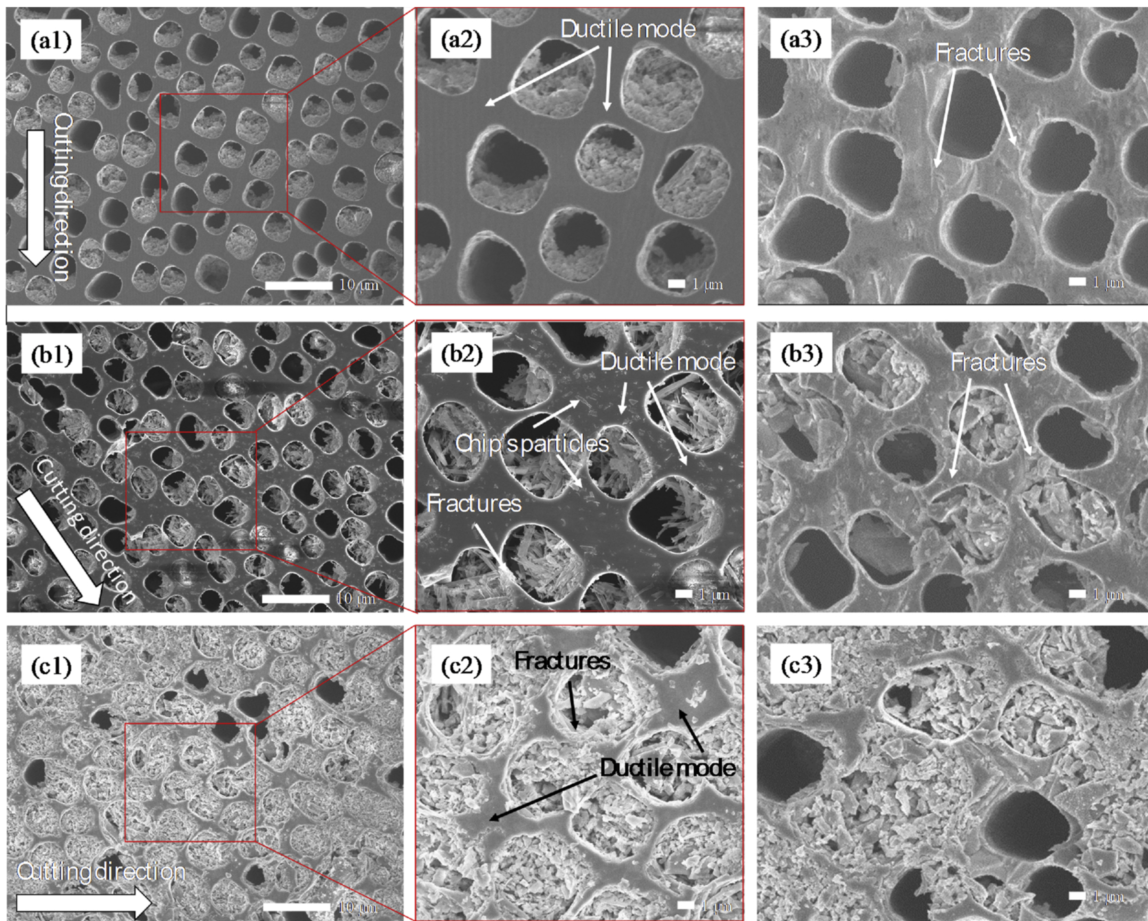

Fig. 5. SEM micrographs of machined surfaces of porous silicon at different maximum undeformed chip thicknesses: (a1, a2, b1, b2, c1 and c2) h_{max} = 30 nm, (a3, b3 and c3) h_{max} = 303 nm and tool rake angles: (a1 ~ 3) α = 0°, (b1 ~ 3) α = −15°, (c1 ~ 3) α = −45°.

NRS-2100 (JASCO Corp., Japan), was used. In addition, to measure cutting forces during the micro/nano-cutting tests a piezoelectric dynamometer (Kistler 9256C2) was fixed below the tool holder.

2.6. Finite element simulation

In this study, a finite element (FE) machining simulation program produced by Third Wave Systems USA (AdvantEdge) was used to simulate the deformation in the cutting area of porous silicon. FE simulation can assist in the better understanding of the effect of rake angle on the material removal mechanism. Simulations were conducted in two-dimensional in orthogonal cutting. Thus, the undeformed chip thickness was considered the same parameter as the depth of cut. Machining conditions used in the simulation were the same as those used in the experiments. The pressure-sensitive Drucker-Prager constitutive model [17–19] was applied to establish the material property model for silicon. The pertinent workpiece material properties are given in Table 1.

3. Results and discussion

3.1. Surface topography

Fig. 5(a1) shows the SEM micrograph of the machined surface of porous silicon at a maximum undeformed chip thickness of 30 nm (f = 0.5 μm/rev and a = 2.0 μm) using a tool with a zero rake angle α. As shown in Fig. 5(a2), at a higher magnification, the surface was cut in ductile mode, and minimum brittle fracture can be observed around pores. Increasing undeformed chip thickness transits the cutting mode from ductile to brittle on the area between pores, leading density and magnitude of the microcracks to increase (Fig. 5(a3)).

Fig. 5(b1) and (b2) show the SEM micrograph of the machined surface of porous silicon using a tool with a negative rake angle (α = −15°). Although surface also cut mostly in ductile mode, there are some areas around pore especially thin wall between the pores where the microfracture occurred. The magnitude of brittle fracture under this condition was also higher than those using a tool with α = 0°, as h_{max} increases (Fig. 5(b3)). Moreover, the surface was covered by chip particles due to the negative rake angle. As the rake angle reached −45°, microfracture around pores was more significant, nevertheless, there are some small areas between pores cut in the ductile mode as shown in Fig. 5(c2).

It is well-known that there is a critical undeformed chip thickness in the ductile cutting of silicon. During the machining of single crystal silicon with less than this critical value, no cracks are generated and cutting process is performed by plastic flow. However, when it exceeds, there is a brittle-ductile transition, leading to generating the microfractures [13,20,21].

The cutting of a brittle material in ductile-mode at room temperature has been explained by several authors based on hydrostatic

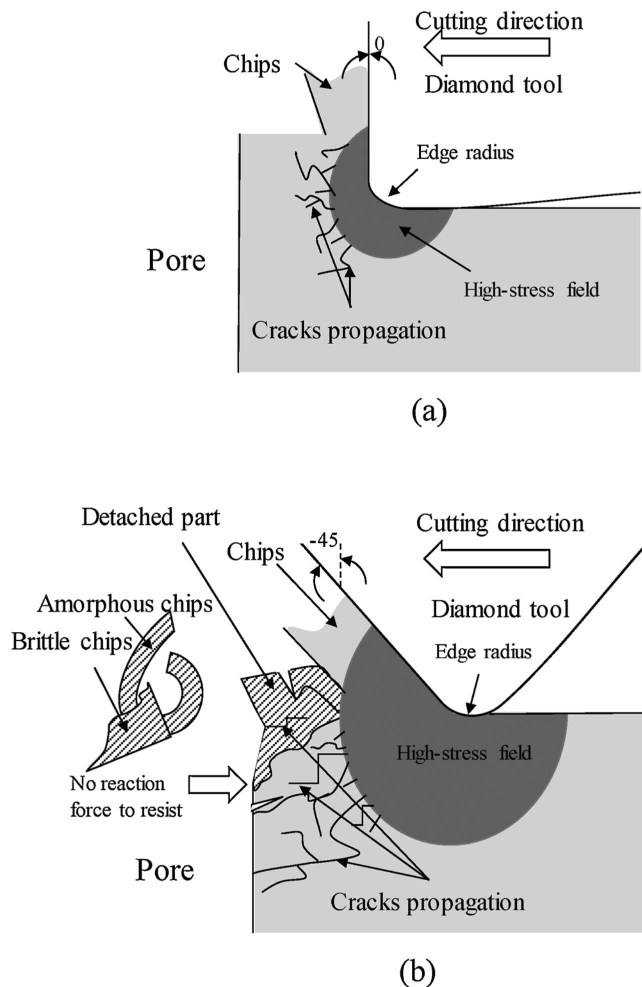

Fig. 6. Schematic illustrations of cutting mechanisms near a pore at two different tool rake angles.

pressure area induced by tool cutting edge [22]. To cut brittle materials in ductile mode, the high pressure is a prerequisite. Such a high compressive stress state can be produced in cutting conditions with the small undeformed chip. This high hydrostatic stress can help to close cracks and prevent microcrack propagation as well [23].

Compared to the machining of single crystal silicon, in porous silicon case, brittle-mode cutting can be observed around pores even at a low h_{max}, while ductile mode was mostly found in the areas among the pores. An increase in h_{max} intensifies the size of brittle fractures. Previous studies by present authors have shown that this phenomenon is due to the high-stress field that cannot be maintained around a pore. The high-stress field propagates microcracks to reach the pore edge, leaving fractures around pores [9]. However, the magnitude of the high-stress region, which can be varied according to tool geometry as well as its effects on the level of brittle fracture, have not been considered.

Tool rake angle significantly influences the magnitude and depth of high-stress field. As schematically shown in Fig. 6(a), in the cutting process using a tool with zero rake angle, high-stress area, induced by the tool edge, initiates crack propagation, but it is too low to extend towards the pore. It needs to be closer to the wall of the pore to cause a brittle fracture. While applying a tool with a negative rake angle considerably induced larger and deeper high-stress region. This provides a condition for microcracks to propagate severely to reach the wall of the pore, leading to a bigger part of silicon to be separated from the pore edge (Fig. 6(b)).

Next, to investigate the effect of tool nose radius on the machined surface, tool nose radii of 0.5 mm, 1.0 mm and 10 mm were considered at the same machining condition. The result of SEM micrograph of surface reveals a very smooth surface when using a tool with $r = 10$ mm compared to the high level of microfracture using a tool with $r = 0.5$ mm (Fig. 7).

Fig. 8 shows a true scale schematic model for face turning with two different tool nose radii. When using the tools with different nose radii at the same machining condition, the important parameter of the maximum undeformed chip thickness will be changed according to nose radius. Increasing tool nose radius decreases h_{max}, which will reduce brittle fractures in the cutting region and consequently the chance of the fracture damage replicating into the plane of the cut surface (Fig. 3).

On the other hand, when the tool moves toward the pore edge, there will be a significant side force component induced by tool feed force, as shown in Fig. 9(a). As a result, the large brittle fractures can be observed around the edge of the pore. Thus, a larger nose radius in the tool can help to reduce this side force component and suppresses brittle fractures (Fig. 9(b)).

Furthermore, a remarkable amount of thin chips cut in ductile-mode are troweled by the rake face of the tool into the edge of pores decreasing pore diameter (Fig. 7(a)).

3.2. Raman spectroscopy

Laser micro-Raman tests were performed on every experimental test to clarify the microstructure of the machined surface in porous silicon samples. In single-crystal silicon (c-Si), the triple degenerate optical phonons reveal in the first-order Raman spectrum at the Raman shift of 521 cm^{-1} while for its amorphous state (a-Si), reflecting optical band peak at 470 cm^{-1} [24,25].

Fig. 10 shows the Raman spectrum of the surfaces machined at $h_{max} = 30$ nm with four different tool rake angles (indicated as ductile-mode cut areas in Fig. 5(a2), (b2), and (c2)). As shown in Fig. 10(a) there is a characteristic Raman peak of c-Si at 521 cm^{-1}, whereas the intensity at other frequencies is negligibly low. This indicates that the structural change in the single crystalline silicon under these conditions was so insignificant that it cannot be detected by the present laser Raman system. Although surface has been cut in ductile mode, just a thin layer formed in an amorphous state and the subsurface layer was mainly crystalline silicon. Usually, the a-Si layer depth increases with the depth of the cut within ductile-mode cutting [20]. As rake angle decreased the a-Si layer depth expands gradually and a broadband peak centered at 470 cm^{-1} appears in Fig. 10c, indicating that the amorphization of the subsurface layer became more significant. This amorphous state reaches the maximum thickness within the laser penetration depth at -45° rake angle (Fig. 10d). Although, as rake angle decreased, ductile-machined areas shrank in the porous silicon samples, the magnitude of the subsurface layer transformed into an amorphous state in these areas rose.

In addition to the a-Si layer thickness, dislocation density and thickness of the dislocation layer may also change with tool rake angle. Previous research revealed that decreasing tool rake angle to -45° increased dislocation density to a maximum [20]. In single-crystal silicon, dislocations are usually oriented along the [1 1 0] directions. Dislocations may occur in the ductile-mode cut area of porous silicon under negative rake angles as well. Unfortunately, dislocations are not

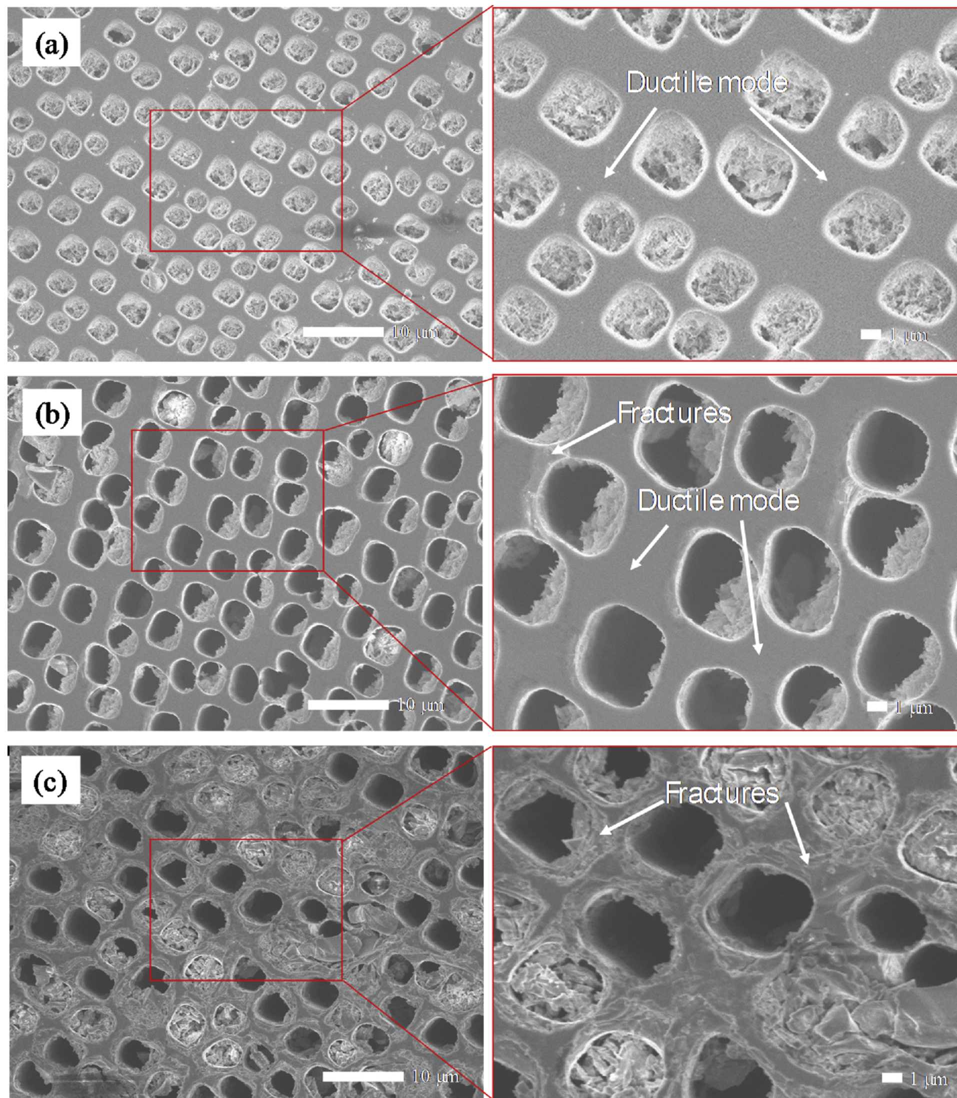

Fig. 7. SEM micrographs of machined surfaces of porous silicon using the different tool nose radii: (a) R = 10.0 mm, (b) R = 1.0 mm, and (c) R = 0.5 mm.

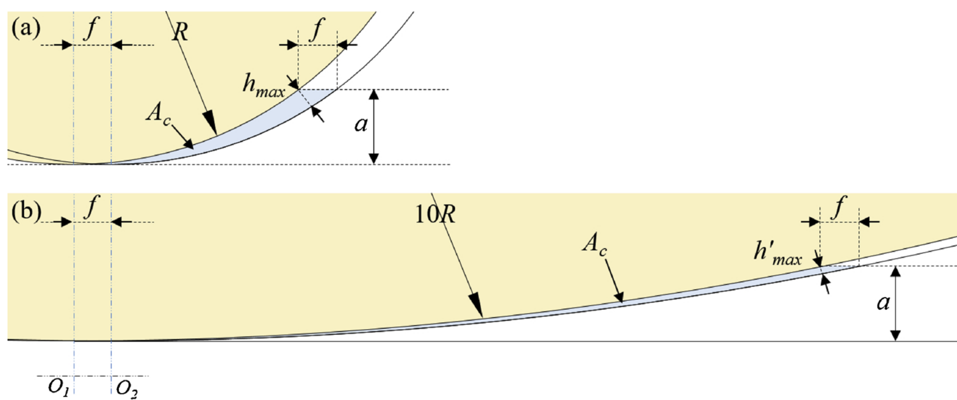

Fig. 8. Schematic model for the undeformed chip cross section (true scale) using two different tool nose radii: (a) R, (b) 10R.

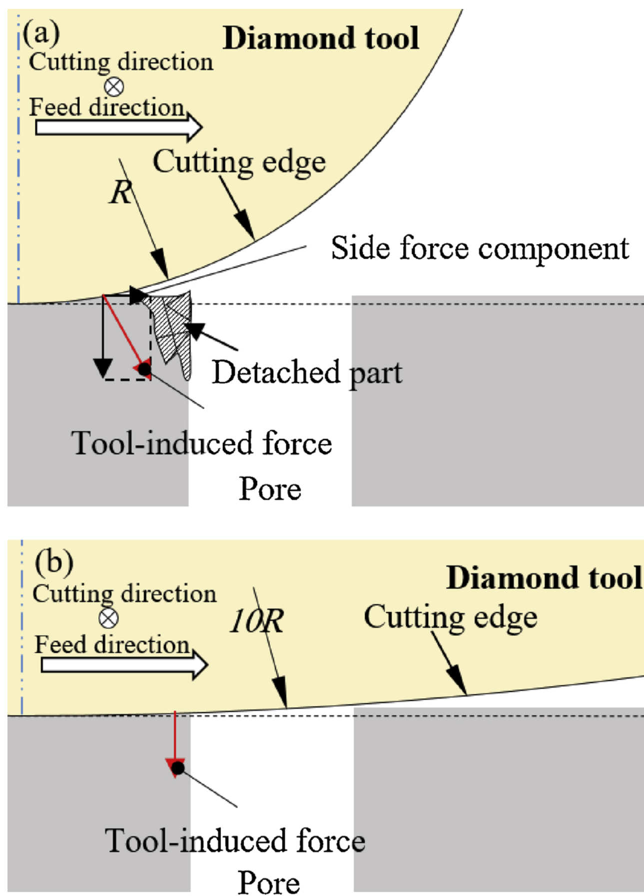

Fig. 9. Schematic illustrations of cutting mechanism near pore using two different tool nose radii: (a) R, (b) $10R$.

detectable by Raman spectroscopy in this study. For future works, subsurface defects of the machined porous silicon will be further investigated using TEM observation.

The results also prove that although increasing tool nose radius to 10 mm decreased undeformed chip thickness to one third, the intensity of the Raman peak of c-Si at 521 cm^{-1} clearly becomes lower (Fig. 11) compared to those of 1.0 mm (Fig. 10(a)).

3.3. Finite element simulation of stress distribution

Fig. 12 shows pressure distributions during the material removal using tools with four different rake angles. The ratio of the depth of cut to tool cutting edge radius is 3:2. Maximum pressure was limited to silicon hardness (H = 13 GPa), therefore, the red area is under compressive stress more than silicon hardness, such a high-stress field is a necessity to machine brittle materials by plastic flow. As FE simulation reveals with decreasing rake angle, high-stress areas, induced by the tool edge, increases that means expanding the amorphous state of subsurface layer. The results of the Raman spectroscopy of the surface already proved increasing amorphization in ductile-mode cut areas as rake angle decreases.

Fig. 13 shows stress distributions obtained using the same tool and under the same machining conditions of those in Fig. 12 as the tool feeds towards a pore edge. In finite element simulations, the compressive yield stress is set equal to the hardness of silicon (H) and tensile yield is set to H/2.2 [26,27]. The results present that a tensile stress

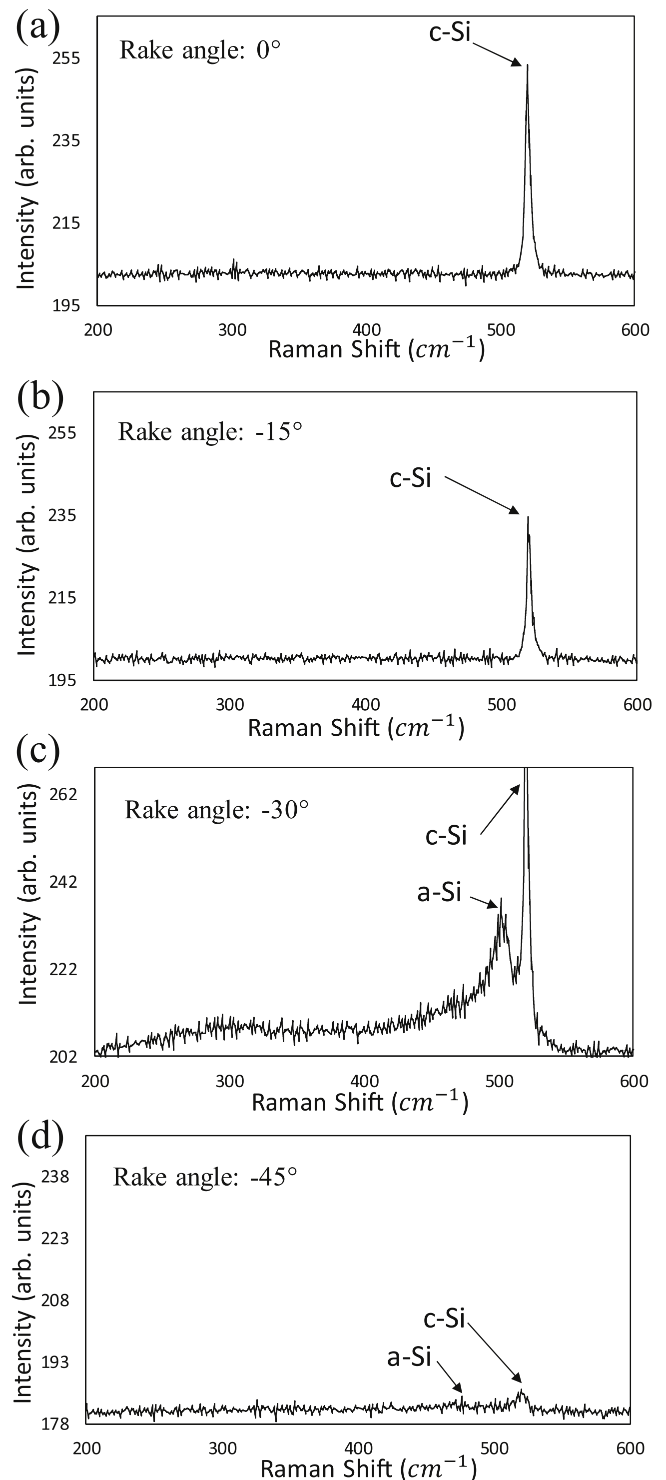

Fig. 10. Laser micro-Raman spectra of ductile-mode machined surface of porous silicon using different tool rake angles: (a) α = 0°, (b) $\alpha = -15°$, (c) $\alpha = -30°$ and (d) $\alpha = -45°$ with R = 1.0 mm at f = 0.5 μm/rev, a = 2.0 μm.

field is generated just beneath the tool tip as the tool moves toward the pore wall inducing microcrack propagation and consequently brittle fractures [9]. As shown in Fig. 13(a), during cutting simulation with zero rake angle this tensile stress is less than the tensile yield stress of

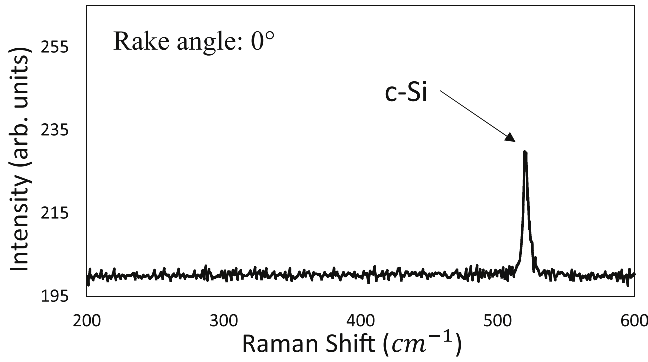

Fig. 11. Laser micro-Raman spectra of the ductile-mode machined surface of porous silicon using a tool with α = 0° and R = 10.0 mm at f = 0.5 μm/rev, a = 2.0 μm.

silicon being too low to cause brittle fractures. In contrast, in negative rake angle, the stress distribution shows the larger area exceeded tensile yield stress. Moreover, as the rake angle decreases, this stress exceeds its yield limitation in the further distance before the tool can reach the pore area. The FE simulation results agreed well with the experimental results, indicating that microfractures around pores increase as rake angle decreases.

3.4. Cutting pressure characteristics

Since the phase transformation of silicon during machining is related to the high contact pressure between the tool tip and the workpiece, the machining pressure P induced by machining force was calculated from the resultant force F_r and the contact area A_r perpendicular to the resultant force as:

$$P = \frac{F_r}{A_r} \tag{2}$$

Where F_r is derived from the measured principal force F_c and thrust force F_t during the experimental tests and A_r was calculated by the following equations:

$$F_r^2 = F_c^2 + F_t^2 \tag{3}$$

$$\tan\gamma = \frac{F_t}{F_C},\ \tan\delta = \frac{A_t}{A_C},\ A_r = A'_r\cos(\gamma - \alpha - \delta) \tag{4}$$

$$A_t = [r(1 - \sin\alpha)] \times \left[2\pi \mathrm{R}\left(\frac{\omega + \psi}{360}\right)\right],\ \tan\psi = \frac{f}{2R},\ \tan\omega = \frac{\sqrt{(2Ra - a^2)}}{(R - a)} \tag{5}$$

(see Fig. 3)

$$\begin{aligned} A_c &= \left(\int_{\frac{f}{2}}^{\sqrt{2Ra-a}} R - \sqrt{R^2 - x^2}\,dx\right) + (f \times a) - \left(\int_{\frac{f}{2}}^{\sqrt{2Ra-a}+f} R - \sqrt{R^2 - (x-f)^2}\,dx\right) \\ &= \left[-\frac{1}{2}R^2\left(\arcsin\left(\frac{x}{R}\right) + \frac{1}{2}\sin\left(2\arcsin\left(\frac{x}{R}\right)\right)\right) + Rx + C_1\right] + [f \times a] \\ &\quad - \left[-\frac{1}{2}R^2\left(\arcsin\left(\frac{x-f}{R}\right) + \frac{1}{2}\sin\left(2\arcsin\left(\frac{x-f}{R}\right)\right)\right) + R(x-f) + C_2\right], \end{aligned} \tag{6}$$

[9]

Where A_c is an effective area of tool rake area during cutting process, A_t is derived from multiplication of effective tool cutting edge radius (r) in the width of chip, A'_r is the resultant area of A_c and A_t, A_r is area of A'_r normal to resultant force, α is tool rake angle and γ is angle between F_r and the horizontal direction. To calculate A_c, integral Eq. (6) can be applied or simply multiplying feed rate f by the depth of cut a (the error is less than 0.01%).

It is worth noting that tool wear has a profound impact on the tool edge radius, and consequently, cutting force increases. In order to decrease the effects of tool wear on pressure results, every tool was used in a very short cutting distance.

In calculating the contact area between the sample and the tool during the cutting process, the porosity percentage of the workpiece might be taken into account (30% porosity). As a result, the effective contact area will be about 70% of the cross-sectional area of the normal chip (Fig. 14).

Fig. 15 shows the machining pressures of porous silicon at three feed rates using different rake angles ranged from 0° to −45°. The result presents that the machining pressure decreases as feed rate increases. Increase in h_{max} with feed rate leading to the machining forces increase, but in the brittle area, the slope of the force increase is significantly lower than that in the ductile area. The material removal in brittle-mode requires smaller cutting forces and consequently less machining pressure. Therefore, it is expected that machining pressure in the cutting of porous silicon should be less than bulk silicon due to the brittle fractures occurring around the pores [9,20]. Machining pressure more than the hardness of silicon occurs at 0.5 μm/rev with zero rake angle indicating that almost entire surface had been cut in ductile mode.

The graph also reveals a very important characteristic of porous silicon cutting that is a significant drop in pressure as rake angle decreases. This trend is completely different from those observed in the machining of non-porous silicon [20]. This phenomenon can be contributed to micofracture occurred around pores in the cutting of porous silicon. As rake angle declines, more brittle fracture occurs around pores that release pressure. However, the most pressure will be concentrated on the area between pore. The area between pore being far from the pore wall will be cut in the severe ductile mode as Raman-spectroscopy results have already shown (Fig. 10).

Next, the effect of the increase in tool nose radius on the machining pressure was considered (Fig. 16). When using a tool with larger nose radius, h_{max} will be decreased, which causes the critical chip thickness h_c to move upward (Fig. 3), leading to higher the ductile cut region [28]. The ductile material removal induces the higher cutting forces. In addition, a decrease in h_{max} may also augment plowing effects, and consequently cutting force increases [29]. Regarding almost same undeformed chip areas, cutting pressure rises in larger tool nose radius.

4. Conclusion

The effects of tool rake angle and nose radius on surface quality of ultraprecision diamond-turned porous silicon were investigated experimentally. The following conclusions were drawn.

(1) Tool rake angle has a profound impact on brittle fracture around pores. As rake angle decreases, the magnitude and depth of high-stress region increases, causing microcracks to propagate around pore walls.
(2) When using a tool with a bigger nose radius, the maximum undeformed chip thickness will be decreased, provided that other conditions are the same, which will reduce brittle fractures in the cutting region. Also, the side-force component is reduced, which suppresses brittle fractures around the pore edge.
(3) Raman spectroscopy of surface showed that as tool rake angle declines the amorphous silicon layer depth expands gradually in ductile-mode cut areas.
(4) Different from the cutting of non-porous silicon, cutting pressure of

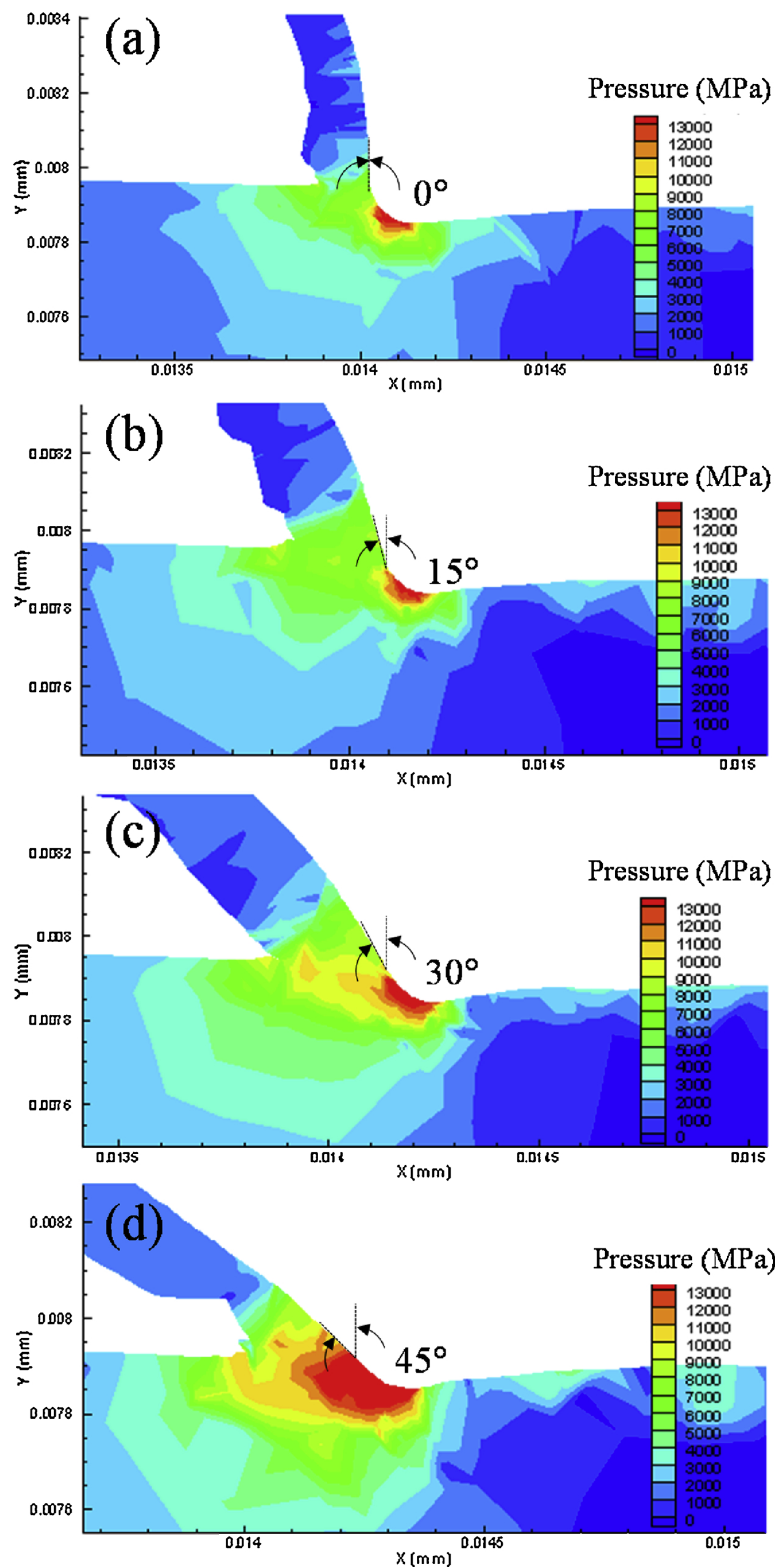

Fig. 12. Pressure distribution in the cutting areas in different tool rake angles: (a) $\alpha = 0^{\circ}$, (b) $\alpha = -5^{\circ}$, (c) $\alpha = -30^{\circ}$ and (d) $\alpha = -45^{\circ}$.

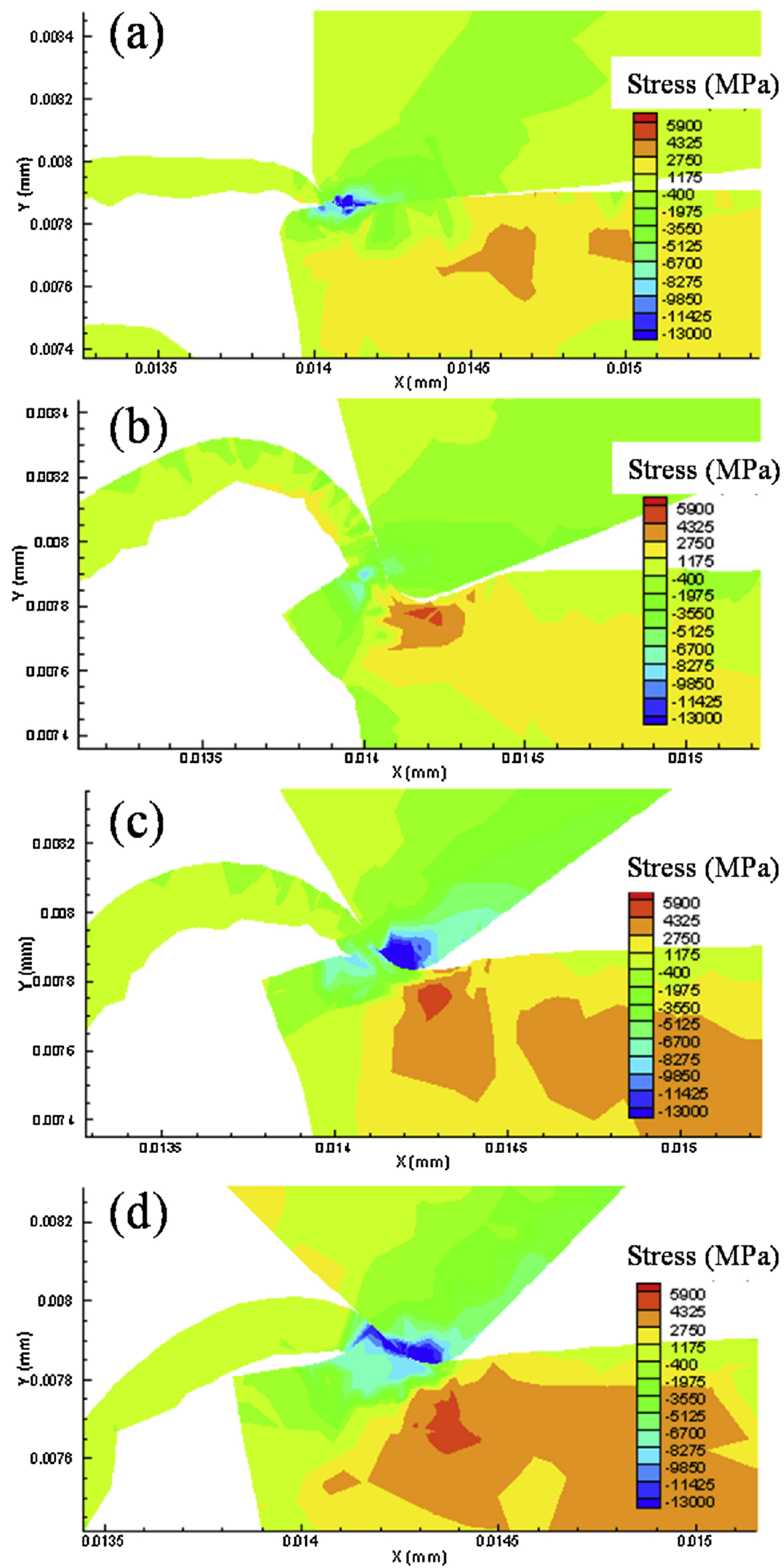

Fig. 13. Stress distribution in the areas near pore in different tool rake angles: (a) $\alpha = 0°$, (b) $\alpha = -15°$, (c) $\alpha = -30°$ and (d) $\alpha = -45°$.

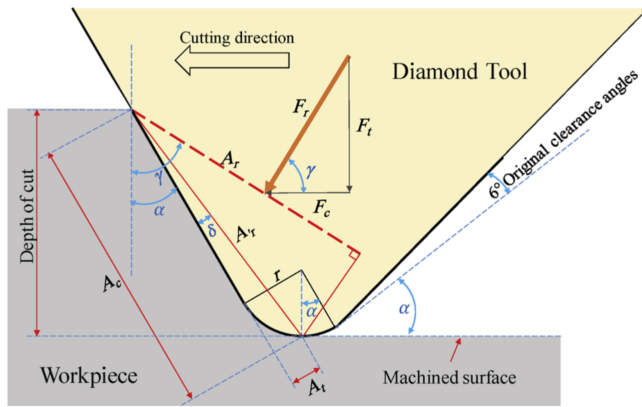

Fig. 14. Model for calculating cutting pressure using a tool with a negative rake angle.

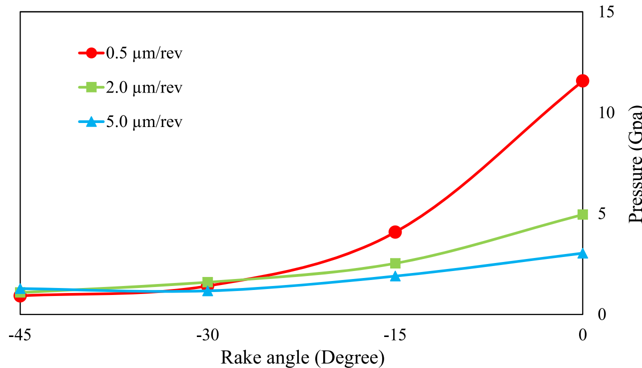

Fig. 15. Changes in cutting pressure with tool rake angle.

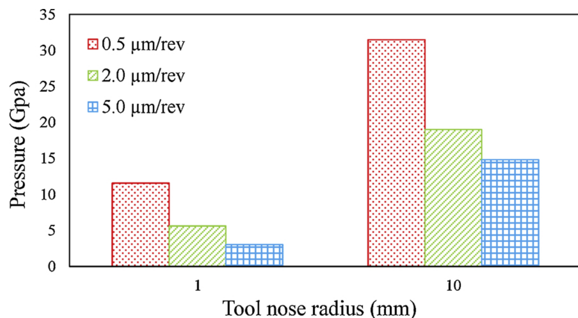

Fig. 16. Changes of cutting pressure with tool nose radius.

porous silicon is reduced as rake angle decreased. As rake angle decreases, more brittle fracture occur around pores that release pressure.

References

[1] Hirschman KD, Tsybeskov L, Duttagupta SP, Fauchet PM. Silicon-based visible light-emitting devices integrated into microelectronic circuits. Nature 1996;384:338–41. https://doi.org/10.1038/384338a0.
[2] Striemer CC, Fauchet PM. Dynamic etching of silicon for broadband antireflection applications. Appl Phys Lett 2002;81:2980–2. https://doi.org/10.1063/1.1514832.
[3] Gowda SR, Pushparaj V, Herle S, Girishkumar G, Gordon JG, Gullapalli H, et al. Three-dimensionally engineered porous silicon electrodes for Li ion batteries. Nano Lett 2012;12:6060–5. https://doi.org/10.1021/nl302114j.
[4] Thakur M, Isaacson M, Sinsabaugh SL, Wong MS, Biswal SL. Gold-coated porous silicon films as anodes for lithium ion batteries. J Power Sources 2012;205:426–32. https://doi.org/10.1016/j.jpowsour.2012.01.058.
[5] Pacebutas V, Grigoras K, Krotkus A. Porous silicon applications in solar cell technology. Phys Scr 1997:255–8. https://doi.org/10.1088/0031-8949/1997/T69/053. T69.
[6] Canham LT. Silicon quantum wire array fabrication by electrochemical and chemical dissolution of wafers. Appl Phys Lett 1990;57:1046. https://doi.org/10.1063/1.103561.
[7] Dubey RS. Electrochemical fabrication of porous silicon structures for solar cells. Nanosci Nanoeng 2013;1:36–40. https://doi.org/10.13189/nn.2013.010105.
[8] Canham L, editor. Handbook of porous silicon Cham: Springer International Publishing; 2014. https://doi.org/10.1007/978-3-319-05744-6.
[9] Heidari M, Yan J. Ultraprecision surface flattening of porous silicon by diamond turning. Precis Eng 2017;49:262–77. https://doi.org/10.1016/j.precisioneng.2017.02.015.
[10] Heidari M, Yan J. Material removal mechanism and surface integrity in ultraprecision cutting of porous titanium. Precis Eng 2018;52:356–69. https://doi.org/10.1016/j.precisioneng.2018.01.014.
[11] Pusavec F. Porous tungsten machining under cryogenic conditions. Int J Refract Met Hard Mater 2012;35:84–9. https://doi.org/10.1016/j.ijrmhm.2012.04.009.
[12] Schoop J, Jawahir IS, Balk TJ. Size effects in finish machining of porous powdered metal for engineered surface quality. Precis Eng 2016;44:180–91. https://doi.org/10.1016/j.precisioneng.2015.12.004.
[13] Yan J, Zhang Z, Kuriyagawa T. Mechanism for material removal in diamond turning of reaction-bonded silicon carbide. Int J Mach Tools Manuf 2009;49:366–74. https://doi.org/10.1016/j.ijmachtools.2008.12.007.
[14] Liu K, Li XP, Rahman M, Neo KS, Liu XD. A study of the effect of tool cutting edge radius on ductile cutting of silicon wafers. Int J Adv Manuf Technol 2007;32:631–7. https://doi.org/10.1007/s00170-005-0364-7.
[15] Dai H, Chen G, Fang Q, Yin J. The effect of tool geometry on subsurface damage and material removal in nanometric cutting single-crystal silicon by a molecular dynamics simulation. Appl Phys A 2016;122:804. https://doi.org/10.1007/s00339-016-0319-x.
[16] Blake PN, Scattergood RO. Ductile-regime machining of germanium and silicon. J Am Ceram Soc 1990;73:949–57. https://doi.org/10.1111/j.1151-2916.1990.tb05142.x.
[17] Ajjarapu SK, Patten JA, Cherukuri H, Brand C. Numerical simulations of ductile regime machining of silicon nitride using the Drucker-Prager material model. Proc Inst Mech Eng Part C-J Mech Eng Sci 2004;218:577–82. https://doi.org/10.1243/095440604774202204.
[18] Patten JA, Jacob J, Bhattacharya B, Grevstad A, Fang N, Marsh ER. Numerical simulations and cutting experiments on single point diamond machining of semiconductors and ceramics. Yan J, Patten J, editors. Semicond. Mach. Micro-nano scale, vol. 661. Kerala, India: Transworld Research Network; 2007. https://doi.org/10.1243/095440604774202204.
[19] Patten JA, Jacob J. Comparison between numerical simulations and experiments for single-point diamond turning of single-crystal silicon carbide. J Manuf Process 2008;10:28–33. https://doi.org/10.1016/j.jmapro.2008.08.001.
[20] Yan J, Asami T, Harada H, Kuriyagawa T. Fundamental investigation of subsurface damage in single crystalline silicon caused by diamond machining. Precis Eng 2009;33:378–86. https://doi.org/10.1016/j.precisioneng.2008.10.008.
[21] Yan J, Asami T, Harada H, Kuriyagawa T. Crystallographic effect on subsurface damage formation in silicon microcutting. CIRP Ann Manuf Technol 2012;61:131–4. https://doi.org/10.1016/j.cirp.2012.03.070.
[22] Patten J, Cherukuri H, Yan J. Ductile-regime machining of semiconductors and ceramics. In: Gogotsi Y, Domnich V, editors. High Press. Surf. Sci. Eng. Taylor & Francis; 2003. p. 543–632. https://doi.org/10.1201/9781420034134.sec6.
[23] Yoshino M, Aoki T, Shirakashi T, Komanduri R. Some experiments on the scratching of silicon: in situ scratching inside an SEM and scratching under high external hydrostatic pressures. Int J Mech Sci 2001;43:335–47. https://doi.org/10.1016/S0020-7403(00)00019-9.
[24] Yan J. Laser micro-Raman spectroscopy of single-point diamond machined silicon substrates. J Appl Phys 2004;95:2094–101. https://doi.org/10.1063/1.1639953.
[25] Gogotsi YG, Baek C, Kirscht F. Raman microspectroscopy study of processing-induced phase transformations and residual stress in silicon. Semicond Sci Technol 1999;14:936–44. https://doi.org/10.1088/0268-1242/14/11/501.
[26] Gilman JJ. Relationship between impact yield stress and indentation hardness. J Appl Phys 1975;46:1435–6. https://doi.org/10.1063/1.321790.
[27] Ajjarapu SK, Fesperman RR, Patten Ja, Cherukuri HP, Brand C. Ductile regime machining of silicon nitride: experimental and numerical analyses. AIP Conf. Proc.. 2014.
[28] Blackley WS, Scattergood RO. Ductile-regime machining model for diamond turning of brittle materials. Precis Eng 1991;13:95–103. https://doi.org/10.1016/0141-6359(91)90500-I.
[29] Chou YK, Song H. Tool nose radius effects on finish hard turning. J Mater Process Technol 2004;148:259–68. https://doi.org/10.1016/j.jmatprotec.2003.10.029.